STEM CELLS

Engineered mesenchymal stromal cells with bispecific polyvalent peptides suppress excessive neutrophil infiltration and boost therapy

Tenghui Ye[1]†, Zixin Wu[2]†, Xi Liu[1], Jiamin Wu[1], Qin Fu[1], Jie Cao[2], Di Zhang[3]*, Peng Shi[1,4,5]*

Excessive neutrophil infiltration can exacerbate inflammation and tissue damage, contributing to conditions like autoimmune disorders and liver diseases. Mesenchymal stromal cells (MSCs) share homing mechanisms with neutrophils, showing promise for treating such diseases. However, ex vivo expanded MSCs often suffer from reduced homing efficiency due to the loss of essential ligands. Here, we engineer MSCs with P-selectin and E-selectin targeting peptides, assembling them into bispecific polyvalent structures using DNA self-assembly technology. This modification allows engineered MSCs to compete with chemotactic neutrophils for selectin binding sites on endothelial cells. In a mouse model of acute liver failure, engineered MSCs effectively home to the damaged liver and substantially inhibit excessive neutrophil infiltration. The combination of inhibiting neutrophil infiltration and the MSCs' inherent therapeutic properties lead to superior therapeutic outcomes. Single-cell RNA sequencing reveals that engineered MSCs elevate the levels of Marco_macrophage, which have neutrophil-inhibitory effects. Our study offers a perspective for advancing MSC-based therapies in tissue repair.

INTRODUCTION

Neutrophil recruitment to sites of inflammation is crucial for maintaining the body's defense mechanisms (*1*). However, dysregulated or excessive neutrophil infiltration can exacerbate inflammation, contributing to various diseases, including autoimmune disorders and liver diseases (*2*, *3*). This aberrant behavior is often characterized by the overproduction of reactive oxygen species (ROS) and neutrophil extracellular traps (NETs), which intensify tissue damage (*4*, *5*). Recent advancements suggest that mitigating excessive neutrophil infiltration holds substantial therapeutic promise (*6*, *7*). For instance, natalizumab, an agent known to attenuate neutrophil-mediated inflammation, is currently used in clinical settings for multiple sclerosis and Crohn's disease. Neutrophil recruitment involves rolling behavior on vascular endothelial cells, mediated by the interaction between P-selectin glycoprotein ligand-1 (PSGL-1) on neutrophils and selectins on activated endothelial cells (*8*). This interaction is crucial for neutrophils to migrate across the endothelial layer and infiltrate damaged tissues. Studies suggest that modulators disrupting this interaction, such as glycopeptide analogs (*9*) or selectin-binding peptides (*10*), have the potential to reduce excessive neutrophil infiltration and tissue damage.

Mesenchymal stromal cells (MSCs) exhibit a homing mechanism similar to that of neutrophils, allowing them to reach damaged tissues and exert therapeutic effects, including immunomodulation, anti-inflammation, and promotion of angiogenesis (*11*, *12*). These properties make MSCs promising candidates for treating autoimmune disorders and liver diseases (*13*). However, ex vivo expanded MSCs often face challenges related to insufficient homing efficiency upon administration, largely due to the loss of homing-related ligands during expansion (*14*, *15*). These MSCs that lose surface ligands also fail to suppress excessive neutrophil infiltration. We hypothesize that modifying the surface of MSCs with selectin-targeting biomolecules, such as peptides and antibodies, could substantially enhance their targeted adhesion to activated vascular endothelial cells. These modified MSCs, exhibiting neutrophil-like homing patterns, are expected to compete with chemotactic neutrophils for selectin binding sites on endothelial cells, thereby reducing excessive neutrophil infiltration. This strategy integrates the inhibition of excessive neutrophil infiltration with enhanced MSCs homing efficiency, potentially leading to improved therapeutic outcomes.

Fundamental studies indicate that P-selectin and E-selectin, present on activated endothelial cells, are crucial receptors facilitating neutrophil-endothelial interactions, regulating the rolling flux and velocity of neutrophils on endothelial surfaces (*16*, *17*). In addition, the dimerization of PSGL-1 is essential for functional interactions with P-selectin (*18*). Inspired by these findings, we modified MSCs with P-selectin and E-selectin targeting peptides. Using DNA self-assembly technology, we assembled the two peptides into bispecific polyvalent structures on the cell surface, mimicking the multivalent interactions of cell adhesion in their native state. This approach leverages the high affinity of the polyvalent structure (*19*) and the synergistic effect of dual targeting peptides to enhance the targeted adhesion of MSCs to vascular endothelial cells. Our study demonstrates that MSCs engineered with bispecific polyvalent peptides exhibit enhanced adhesion to vascular endothelial cells and superior inhibition of neutrophil infiltration, both in vitro and in vivo. In a mouse model of acute liver failure (ALF), engineered MSCs substantially mitigate liver damage caused by excessive neutrophil infiltration, improve the immune microenvironment of liver tissue, thereby promoting effective liver tissue repair. Furthermore, single-cell RNA

[1]School of Biomedical Sciences and Engineering, South China University of Technology, Guangzhou International Campus, Guangzhou 511442, PR China. [2]Department of General Surgery, Guangzhou Digestive Disease Center, the Second Affiliated Hospital, School of Medicine, South China University of Technology, Guangzhou, Guangdong 510180, China. [3]Department of General Surgery (Colorectal Surgery), Guangdong Provincial Key Laboratory of Colorectal and Pelvic Floor Diseases, Guangdong Institute of Gastroenterology, Biomedical Innovation Center, The Sixth Affiliated Hospital, Sun Yat-sen University, Guangzhou 510655, China. [4]National Engineering Research Center for Tissue Restoration and Reconstruction, South China University of Technology, Guangzhou 510006, PR China. [5]Guangdong Provincial Key Laboratory of Biomedical Engineering, South China University of Technology, Guangzhou 510006, PR China.
*Corresponding author. Email: pxs301@scut.edu.cn (P.S.); zhangdi@mail2.sysu.edu.cn (D.Z.)
†These authors contributed equally to this work.

sequencing (scRNA-seq) analysis reveal that bispecific polyvalent peptide-engineered MSCs elevate the levels of Marco_macrophage, which have neutrophil-inhibitory effects. This cell engineering strategy offers a perspective for advancing MSC-based therapies in tissue repair.

RESULTS

Synthesis of bispecific polyvalent peptides via DNA template–directed molecular assembly

DNA has become a versatile tool for assembling biomolecules into complex structures (*20*, *21*). In this study, we used DNA template–directed molecule assembly to create bispecific polyvalent peptides. The set of DNA sequences included a DNA initiator (DI) and two hairpin-like DNA monomers (DMs), DM1 and DM2. In the presence of DI, DM1 and DM2 self-assemble into a DNA polymer through a hybridization chain reaction (HCR) (fig. S1) (*22*). Thus, by conjugating P-selectin binding peptide (PBP) and E-selectin binding peptide (EBP) with DM1 and DM2, respectively, the peptides are programmed into polyvalent structures via HCR (Fig. 1A). To prepare the DNA-peptide conjugate, amino-modified DNA was reacted sequentially with N-hydroxysuccinimide-dibenzocyclooctyne (NHS-DBCO) cross-linker and azide-modified peptide, resulting in the formation of DM1-PBP and DM2-EBP. The conjugates were purified using high-performance liquid chromatography (HPLC) (Fig. 1B). The ultraviolet-visible (UV-vis) absorption spectrum of the DNA-peptide conjugate displayed the characteristic DNA absorption peak at 260 nm. In addition, with the peptide fluorescently labeled [fluorescein isothiocyanate (FITC) or Rhodamine], the fluorescence emission spectrum of the DNA-peptide conjugate revealed the characteristic emission peak of peptide-fluorophore, indicating successful coupling of DNA and the peptide (Fig. 1C).

For the polymerization of DNA-peptides into polyvalent structures, DM1-PBP-FITC, DM2-EBP-Rhodamine, and DI were incubated for 3 hours in a neutral buffer. Gel electrophoresis images demonstrated that the linkage between DNA and peptides did not hinder the self-assembly of DMs into polymers (Fig. 1D) and that the peptides bound to DNA were successfully assembled into polyvalent structures (Fig. 1E). Furthermore, the polymers had apparent molecular weights ranging from 500 to 900 base pairs, corresponding to 9 to 14 DM1-PBP and 9 to 14 DM2-EBP units per bispecific peptide (fig. S2A), with an average size of 261 nm as determined by a nanoparticle size analyzer (fig. S2B). To assess whether polyvalent peptides had superior binding to activated endothelia cells compared to their monovalent counterparts, we determined the apparent dissociation constant (i.e., K_d) for the binding of polyvalent peptides to activated human umbilical vein endothelial cells (HUVECs). The K_d values for monovalent selectin-binding peptides were 1140 nM for PBP and 1069 nM for EBP. Upon assembly into polyvalent peptides via DNA assembly, these K_d values were substantially reduced (fig. S3). For instance, the K_d value for the polyvalent PBP was 268 nM, comparable to the natural PSGL-1 binding to P-selectin (320 nM) (*23*). This indicates a notably higher binding affinity of polyvalent peptides to target cells compared to monovalent peptides.

Construction of engineered MSCs

We then investigated the synthesis of bispecific polyvalent peptides directly on the MSC surface. As depicted in Fig. 1F, a cholesterol-ended

DI was embedded into the cell membrane through hydrophobic interaction, thereby anchoring the oligonucleotide on the cell surface. Subsequently, the MSCs were incubated with DM1-PBP and DM2-EBP to prepare polyvalent P-selectin and E-selectin binding peptide-engineered MSCs (PPE-MSCs). We also prepared several control groups. To highlight the benefits of polyvalent interactions in enhancing MSC adhesion, we included a control group of monovalent P-selectin and E-selectin binding peptide-engineered MSCs (MPE-MSCs) (fig. S4A). Confocal fluorescence imaging confirmed the successful modification of MSC surfaces with polyvalent peptides (Fig. 1G). Flow cytometry analysis further validated the assembly of polyvalent peptides on MSCs. Fluorescence intensity quantification revealed an eightfold increase in the fluorescence intensity of FITC and Rhodamine in PPE-MSCs compared to MPE-MSCs (Fig. 1H), indicating an average of eight PBP and eight EBP on each bispecific polyvalent structure, consistent with gel electrophoresis results. Moreover, we precisely quantified the number of peptides on the engineered PPE-MSC surface (table S2). For instance, at 1 μM DI, the density of polyvalent structure was ~2.4×10^7 units per cell, corresponding to 1.9×10^8 EBPs and 1.9×10^8 PBPs. We then assessed the stability of both monovalent and polyvalent surface modifications. After 24 hours of exposure to serum-containing culture medium, PPE-engineered cells retained ~25% of the surface peptides, whereas MPE-engineered cells maintained only about 5% of the surface peptides (fig. S5).

To clarify the synergistic effect of dual targeting peptides in promoting the targeted adhesion of MSCs, we prepared control groups of polyvalent P-selectin peptide-engineered MSCs (PP-MSCs) and polyvalent E-selectin peptide-engineered MSCs (PE-MSCs) (fig. S4, B and C). Confocal fluorescence imaging and flow cytometry analysis confirmed the successful modification of MSC surfaces with polyvalent peptides. Fluorescence intensity quantification revealed that each polyvalent structure on PP-MSCs contains 16 PBPs, whereas each structure on PE-MSCs contains 16 EBPs. The number of peptides on the cell surface was also quantified (table S3). For instance, at 1 μM DI, each PP-MSC displayed 3.8×10^8 PBPs on its surface. Under the same DI concentration, the total peptide number on the surface of PP-MSCs is equivalent to that on the surface of PPE-MSCs.

Impact of cell surface modification on MSC functions and in vivo biosafety

Following the successful assembly of polyvalent peptides on MSCs, we investigated the impact of this modification on MSC function. First, we analyzed MSC gene expression using quantitative polymerase chain reaction (qPCR). The expression levels of apoptosis-related genes (*Notch1* and *P53*) and differentiation-related genes (*Alp*, *Ocn*, *Fabp4*, *Pparγ*, *Col2a1*, and *Sox9*) in engineered MSCs after 24 hours of culture showed no notable differences compared to native MSCs (fig. S6A). In addition, the supernatant from engineered MSCs cultured for 3 days was collected for enzyme-linked immunosorbent assay (ELISA) to assess paracrine factor secretion. The results indicated that peptide modification did not affect the secretion of several key paracrine factors [hepatocyte growth factor (HGF), stromal cell–derived factor 1 (SDF-1), monocyte chemoattractant protein 1 (MCP-1), interleukin-6 (IL-6), and transforming growth factor–β (TGF-β1)] compared to native MSCs (fig. S6B). These findings suggest that surface modification preserves the therapeutic efficacy of MSCs. Furthermore, CCK-8 experiments demonstrated that the proliferation ability of engineered MSCs was comparable to that of native MSCs (fig. S6C). Live-dead staining
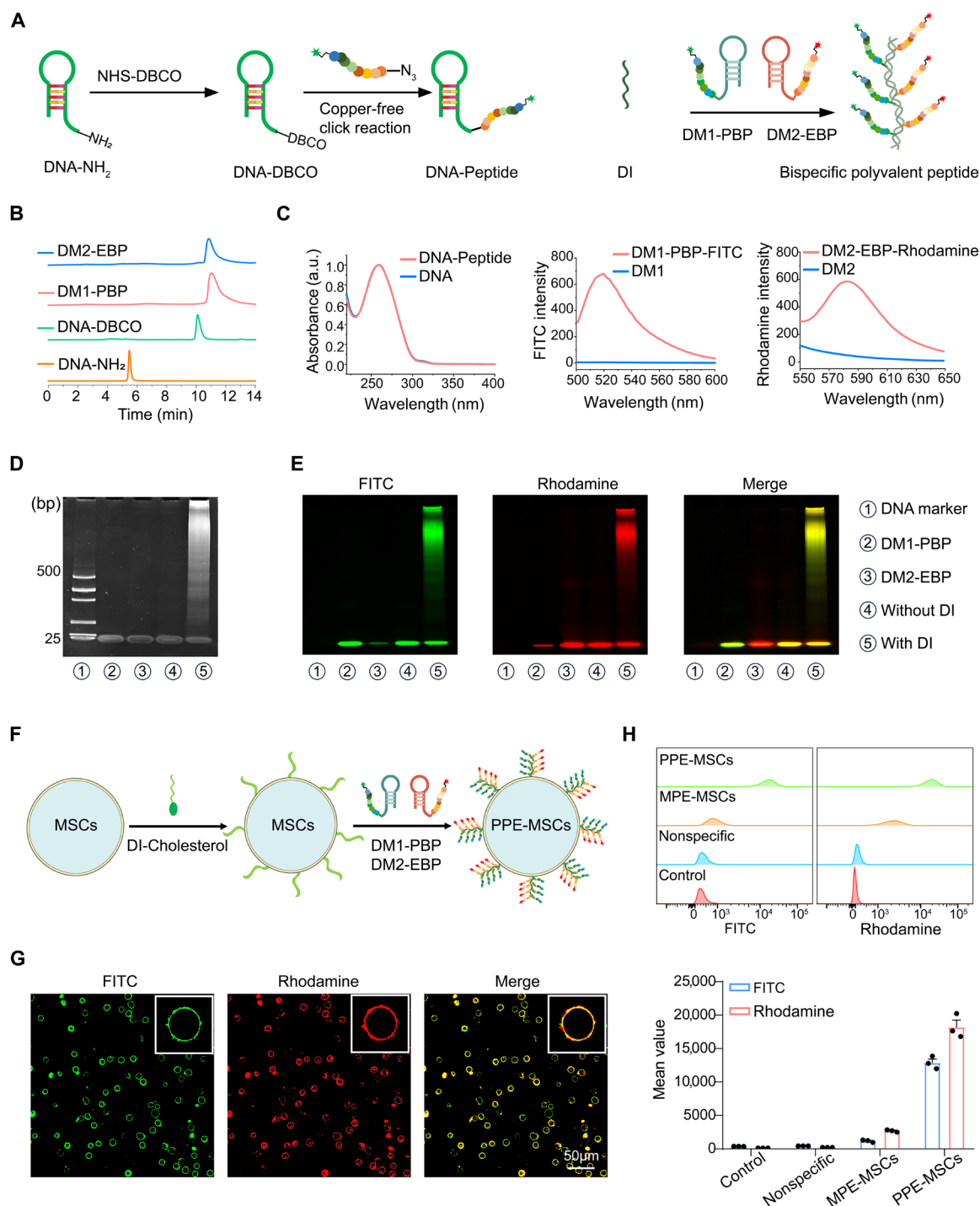
Fig. 1. Synthesis and characterization of bispecific polyvalent peptides and PPE-engineered MSCs. (**A**) Schematic illustration of the preparation process for bispecific polyvalent peptide. (**B**) HPLC analysis of DNA-NH$_2$, DNA-DBCO, DM1-PBP, and DM2-EBP. (**C**) UV-vis absorption spectra (left) and fluorescence emission spectra (right) of DNA-peptide conjugates. (**D**) Gel electrophoresis imaging for the characterization of DNA-peptide assembly. bp, base pairs. (**E**) Gel electrophoresis imaging for the characterization of polyvalent peptides. (**F**) Schematic illustration of the bottom-up assembly of bispecific polyvalent peptides on MSC surface. (**G**) Confocal fluorescence image of PPE-engineered MSCs. (**H**) Flow cytometry analysis of fluorescence intensity in MPE-MSCs and PPE-MSCs. Means ± SEM, $n = 3$ independent replicates. The fluorescent signal was detected by confocal microscopy or flow cytometry immediately after the engineered cells were assembled. DI, DNA initiator; DM1, DNA monomers 1; DM2, DNA monomers 2; PBP, P-selectin binding peptide; EBP, E-selectin binding peptide; MPE-MSCs, monovalent P-selectin and E-selectin binding peptide-engineered MSCs; PE-MSCs, polyvalent E-selectin peptide-engineered MSCs; PP-MSCs, polyvalent P-selectin peptide-engineered MSCs; PPE-MSCs, polyvalent P-selectin and E-selectin binding peptide-engineered MSCs.

revealed that peptide modification did not compromise MSC survival, with cells exhibiting stable growth (fig. S6D). Collectively, these results confirm that the polyvalent peptides are biocompatible for MSC surface modifications and do not affect MSC fundamental functions.

We also assessed the biosafety of engineered MSCs in vivo. After intravenous infusion of engineered MSCs into healthy mice, whole blood and spleen samples were collected to assess T cell activation. Flow cytometry analysis indicated that neither native MSCs nor engineered MSCs induced T cell activation in the blood or spleen of mice (fig. S7, A and B). In addition, there were no abnormal increases in biochemical factors in the blood of mice (fig. S7C). These findings suggest that polyvalent peptide modification maintains the low immunogenicity of MSCs and does not trigger adaptive immunity activation in mice. Furthermore, monitoring the mice's weights over 14 days after engineered MSC treatment revealed no notable deviations from normal. After 14 days, hearts, livers, spleens, lungs, and kidneys were collected from the mice, and hematoxylin and eosin (H&E) staining experiments showed no visible tissue damage in these organs (fig. S8). Together, these experimental results confirm the favorable biosafety profile of engineered MSCs in vivo.

Targeted adhesion and neutrophil antagonism of engineered MSCs

After confirming the favorable biosafety profile of engineered MSCs, we investigated whether modifying selectin-binding peptides could enhance MSCs' targeted adhesion and their ability to inhibit neutrophil infiltration. To mimic inflamed endothelium, we pretreated HUVECs with tumor necrosis factor–α (TNF-α) to induce selectin overexpression. Native MSCs or engineered MSCs were then coincubated with pretreated HUVECs. Fluorescence images revealed that the modification of selectin-binding peptides on the cell surface enhanced MSC adhesion to HUVECs (Fig. 2A). Furthermore, the number of MSCs engineered with polyvalent peptides that adhered to HUVECs substantial exceeded those engineered with monovalent peptides, indicating that polyvalent interactions enhance the cell binding. Notably, the number of adhered cells in the PPE-MSCs group exceeded those in both the PP-MSCs and PE-MSCs groups, demonstrating the additive effect of bispecific peptides in enhancing MSC adhesion. Next, we introduced additional control groups, PP-MSCs[half] and PE-MSCs[half]. In comparison to the polyvalent structure on PPE-MSCs, which contains eight PBPs and eight EBPs, the polyvalent structure on PP-MSCs[half] contains eight PBPs, and the polyvalent structure on PE-MSCs[half] contains eight EBPs, as shown in fig. S9 (A and B). When these engineered MSCs were incubated with HUVECs, we observed that the number of adherent cells in the PPE-MSCs group was greater than the combined total of the PP-MSCs[half] and the PE-MSCs[half] group (fig. S9C). In other words, the combined effect of PBPs and EBPs is greater than the sum of their individual effects. On the basis of the performance of engineered MSCs with different peptide configurations, we demonstrate that the bispecific polyvalent peptides exert a synergistic effect in enhancing MSC adhesion.

We further evaluated the effect of PPE modification density on MSC adhesion. Results showed that the number of PPE-MSCs adhering to HUVECs increased proportionally with the increase in PPE modification density, peaking at a PPE density of 2.4×10^7 (fig. S10). In addition, we performed a flow adhesion experiment under well-defined shear conditions to assess the rolling velocity of PPE-MSCs

on HUVECs. The results indicated that the rolling velocity of PPE-MSCs on HUVECs was 5.5 μm/s, which is 5.8 times lower than that of native MSCs. Notably, this rolling velocity is comparable to that of neutrophils observed in inflammatory foci in a previous study (24) (fig. S11).

Next, we investigated the antagonistic effect of engineered MSCs on neutrophils. After the adhesion of engineered MSCs to HUVECs, HL60 cells (mimicking neutrophils) were introduced. Fluorescence images revealed a gradual reduction in HL60 cells (red cells) adhering to HUVECs as the number of engineered MSCs (green cells) adhering to HUVECs increased. Notably, we found the fewest HL60 cells adhered to HUVECs in the PPE-MSCs group (Fig. 2B). The effect was also observed when the engineered MSCs were coincubated with HL60 cells, with PPE-MSCs demonstrating the strongest antagonistic effect on HL60 cell adhesion (fig. S12). This suggests that, as more MSCs adhere to endothelial cells, they occupy binding sites that would otherwise bind neutrophils, thereby effectively antagonizing neutrophil adhesion to endothelial cells. In addition, to expand the applicability of our engineered cell method, we used bispecific polyvalent peptides to modify human MSCs (hMSCs). The results demonstrated that PPE modification could be successfully applied to hMSCs, enhancing their adhesion to vascular endothelial cells and improving their ability to inhibit neutrophil adhesion (fig. S13).

We proceeded to use a mouse model of acute ear inflammation to assess the in vivo performance of engineered MSCs. In this model, lipopolysaccharide (LPS) was subcutaneously injected into the right ear of the mouse to induce inflammation, whereas saline served as a control injected into the left ear (25). MSCs were stained with Vybrant-DiD for in vivo tracking and intravenously administered to the mice. In vivo imaging system (IVIS) imaging of the mouse ears revealed that MSCs homed specifically to the inflamed right ear, with minimal fluorescence in the left ear (fig. S14A). Consistent with in vitro findings, the PPE-MSCs group showed higher cell homing to damaged ears compared to other groups (fig. S14B), suggesting that bispecific polyvalent peptide modification can enhance the specific delivery of MSCs to inflammatory sites more efficiently. Moreover, we conducted immunofluorescence staining on the right ears of mice to examine the targeted adhesion of engineered MSCs to vascular endothelial cells and the neutrophil infiltration in damaged tissues. The results revealed that MSCs could colocalize with vascular endothelial cells and penetrate into surrounding tissue. The PPE-MSCs group had the highest number of MSCs adhering to vascular endothelial cells compared to other groups, indicating that the modification with bispecific polyvalent peptides substantially enhanced the targeted adhesion of MSCs to inflamed vascular endothelial cells (fig. S14C). Immunostaining for neutrophils showed a substantial reduction in neutrophil infiltration in the damaged ears of mice treated with PPE-MSCs, suggesting that PPE-MSCs effectively mitigate neutrophil infiltration in vivo.

Engineered MSCs homing to the damaged liver in ALF mice

After demonstrating the efficacy of PPE-MSCs in targeted adhesion and neutrophil antagonism both in vivo and in vitro, we further assessed the therapeutic potential of engineered MSCs in an ALF mouse model. Currently, liver transplantation is the only effective treatment for ALF (26). However, the scarcity of donors and high costs necessitate exploring alternative treatment options. MSCs are recognized for their potential to modulate immune responses, inhibit apoptosis, and
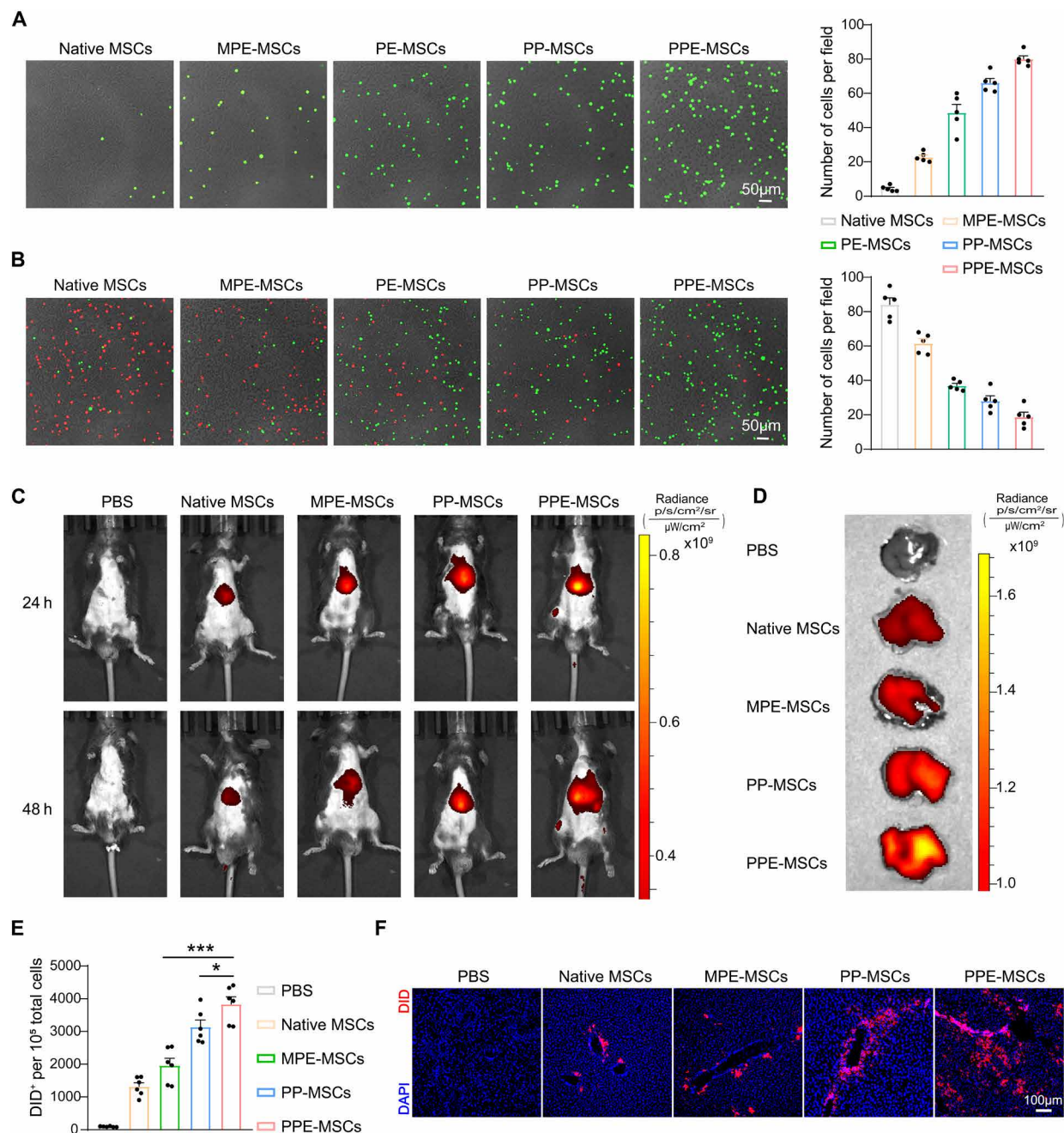
Fig. 2. In vivo and in vitro characterization of targeted adhesion in engineered MSCs. (A) Representative fluorescence images (left) and quantitative analysis (right) showing the adhesion of engineered MSCs to HUVECs. Means $\pm$ SEM, $n = 5$ independent experiments. Representative images out of five images obtained are shown. (**B**) Representative fluorescence image (left) and quantitative analysis (right) illustrating the antagonism of engineered MSCs against HL-60 cells. Means $\pm$ SEM, $n = 5$ independent experiments. Representative images out of five images obtained are shown. (**C**) IVIS imaging of ALF mice treated with native or engineered MSCs. Mice were anesthetized at 24 and 48 hours post-MSC injection and imaged using the IVIS Lumina Series III. $n = 6$ mice. h, hours. (**D**) IVIS imaging of ALF mouse livers posttreatment. Mice were euthanized 24 hours post-MSC injection, and livers were immediately removed for imaging. $n = 6$ mice. (**E**) Quantitative analysis of MSC retention in the liver. Bar chart represents the number of DiD$^+$ cells out of 1×10^5 total cells collected from ALF mouse liver 24 hours postinjection. Means $\pm$ SEM. $n = 6$ mice. (**F**) Immunofluorescence staining of liver tissue to assess MSC homing. Representative images out of seven images obtained are shown. MPE-MSCs, monovalent P-selectin and E-selectin binding peptide-engineered MSCs; PE-MSCs, polyvalent E-selectin peptide-engineered MSCs; PP-MSCs, polyvalent P-selectin peptide-engineered MSCs; PPE-MSCs, polyvalent P-selectin and E-selectin binding peptide-engineered MSCs. Statistical analysis was performed by two-way ANOVA with Tukey's multiple comparisons tests ($*P < 0.05$; $***P < 0.001$).

alleviate oxidative stress, making them a promising alternative for ALF therapy (*27, 28*). In this study, we used an acetaminophen (APAP)–induced mouse model of ALF (*29*). We first validated the establishment of APAP-induced ALF mouse model. Injection of APAP (500 mg/kg) resulted in over 50% mortality in mice within 72 hours, with alanine aminotransferase (ALT) and aspartate aminotransferase (AST) levels in mouse serum rising rapidly within 12 hours and peaking at 24 hours. Histological examination of mouse liver tissue revealed extensive necrosis. These findings confirm that a dose of 500 mg/kg APAP induces severe liver necrosis, with peak severity at 24 hours, consistent with the existing literature (fig. S15, A to C).

Engineered MSCs were intravenously injected into mice 6 hours after APAP administration, and IVIS imaging was performed at 24 and 48 hours postinfusion to observe MSC homing to the damaged liver. As shown in Fig. 2C, MSC accumulation in the damaged liver was greater at 24 hours compared to 48 hours. Notably, the group receiving PPE-MSCs exhibited the highest number of MSCs homing to the liver tissue compared to other groups (Fig. 2D and fig. S16). To obtain more quantitative information, flow cytometry analysis was used to quantify the MSC population in mouse liver, revealing that the number of PPE-MSCs homing to the damaged liver was 3.0 times greater than that of native MSCs (Fig. 2E). Biodistribution experiments performed on ALF mice showed substantial MSC accumulation in the lungs. However, engineered MSCs exhibited reduced retention in the lungs compared to native MSCs, with increased cell numbers detected in the liver (fig. S17). Furthermore, immunofluorescence staining of liver tissue illustrated the gradual spread of MSCs from the vascular lumen to surrounding tissues (Fig. 2F). Collectively, these experiments demonstrate that surface modification of MSCs with bispecific polyvalent peptides substantially enhances their targeted adhesion to the damaged liver in ALF mice.

Attenuation of neutrophil infiltration by engineered MSCs in damaged livers

Excessive intake of APAP can lead to intracellular oxidative stress, mitochondrial dysfunction, and DNA damage. This sequence of events triggers inflammation via damage-associated molecular patterns, which, in turn, recruits a substantial number of neutrophils to the liver, intensifying hepatocyte apoptosis (*30–32*). Our study examined neutrophil infiltration in the livers of ALF mice following treatment with engineered MSCs (Fig. 3A). We administered phosphate-buffered saline (PBS), native MSCs, or engineered MSCs to ALF mice and harvested their livers for examination after 24 hours. Compared to the healthy control group, the livers of ALF mice showed obvious edema and a pale appearance. In contrast, the livers of mice treated with engineered MSCs exhibited a uniformly dark brown color, indicating reduced damage (fig. S18). We subsequently isolated immune cells from liver tissues and quantified the neutrophil population using flow cytometry. The results showed that neutrophils constituted 24.8% of CD45$^+$ cells in the PBS group, indicating rapid neutrophil infiltration into the damaged liver. In contrast, the proportion of neutrophils in mice injected with engineered MSCs was substantially lower, with the PPE-MSCs group showing the lowest proportion at ~2.5% of CD45$^+$ cells (Fig. 3, B and C). We proceeded to quantify the specific number of neutrophils infiltrating the liver. In the PBS group and native MSCs group, there were 14.7×10^5 and 10.0×10^5 neutrophils per gram of liver tissue, respectively. Notably, the PPE-MSCs group exhibited only 1.4×10^5 neutrophils per gram of liver tissue, which was remarkably reduced by 10.6 times compared to the PBS group (Fig. 3D). Quantitative

immunohistochemical analysis also showed that engineered MSC treatment substantially reduced neutrophil infiltration, with the PPE-MSCs group showing the least neutrophil accumulation (Fig. 3, E and F). The above quantitative data demonstrate the effectiveness of PPE-MSCs in reducing neutrophil infiltration. To highlight the benefits of MSC surface modification strategy for inhibiting neutrophil infiltration, we further investigated neutrophil infiltration in the damaged liver following coadministration of MSCs and PPE and compared the results to those from the PPE-MSCs group. The findings revealed that neutrophil infiltration was substantially higher in the coadministration group than in the PPE-MSCs group, emphasizing the necessity and effectiveness of PPE modification for MSC engineering in enhancing neutrophil suppression (fig. S19).

CXCL1-CXCR1 and CXCL2-CXCR2 are crucial chemokine-receptor pairs involved in neutrophil recruitment and activation during inflammation (*33*). CXCL1 and CXCL2, secreted by cells like endothelial cells and macrophages in response to inflammation, bind to their receptors, CXCR1 and CXCR2, on neutrophils. This binding initiates signaling that mediates neutrophil chemotaxis and activation, directing them to inflamed or injured tissue. Thus, we used qPCR to assess CXCR1 and CXCR2 gene expression levels in liver tissue and ELISA to quantify CXCL1 and CXCL2 protein concentrations in serum. Comparative analysis revealed that the PPE-MSCs group exhibited substantially reduced CXCR1 and CXCR2 gene expression in liver tissue compared to control and other treatment groups (Fig. 3G). Correspondingly, serum levels of CXCL1 and CXCL2 were notably lower in the PPE-MSCs group (Fig. 3H). The decreased expression of CXCR1 and CXCR2 could be attributed to the reduced number of neutrophils in liver tissue after PPE-MSCs treatment. Furthermore, the decreased levels of CXCL1 and CXCL2 indicate inhibition of the neutrophil recruitment process, highlighting the beneficial role of PPE-MSCs in attenuating neutrophil infiltration. Infiltrating neutrophils produce substantial ROS and NETs, which exacerbate liver damage. Therefore, we assessed both ROS and NETs levels in the injured liver. The results revealed a substantial increase in ROS accumulation and NETs formation in the PBS group, explaining the severe liver damage observed in that group. In contrast, mice treated with PPE-MSCs showed a substantial reduction in both ROS and NETs levels, indicating a decrease in tissue damage and highlighting the protective effect of PPE-MSCs in the injured liver (Fig. 3I). Together, MSCs engineered with bispecific polyvalent peptides demonstrate efficacy in reducing neutrophil infiltration into damaged liver tissue, ameliorating tissue damage caused by excessive neutrophil infiltration.

Enhanced therapeutic efficacy of engineered MSCs against ALF

Motivated by the superior targeted adhesion and neutrophil antagonism abilities of PPE-MSCs, we investigated the therapeutic efficacy of engineered MSCs in ALF mice. First, we monitored the survival status of mice over a 7-day period. The mortality rate of mice in the PBS group reached 70%, whereas treatment with native MSCs or engineered MSCs notably decreased the mortality rate. Particularly, mice receiving PPE-MSCs exhibited the lowest mortality rate at 10% (Fig. 4A). We then evaluated the serum levels of ALT and AST in ALF mice from day 1 to day 4 posttreatment. Mice treated with MSCs showed lower ALT and AST levels compared to the PBS group, indicating a therapeutic effect of MSCs on APAP-induced liver injury (Fig. 4, B and C). In particular, ALT and AST levels in the
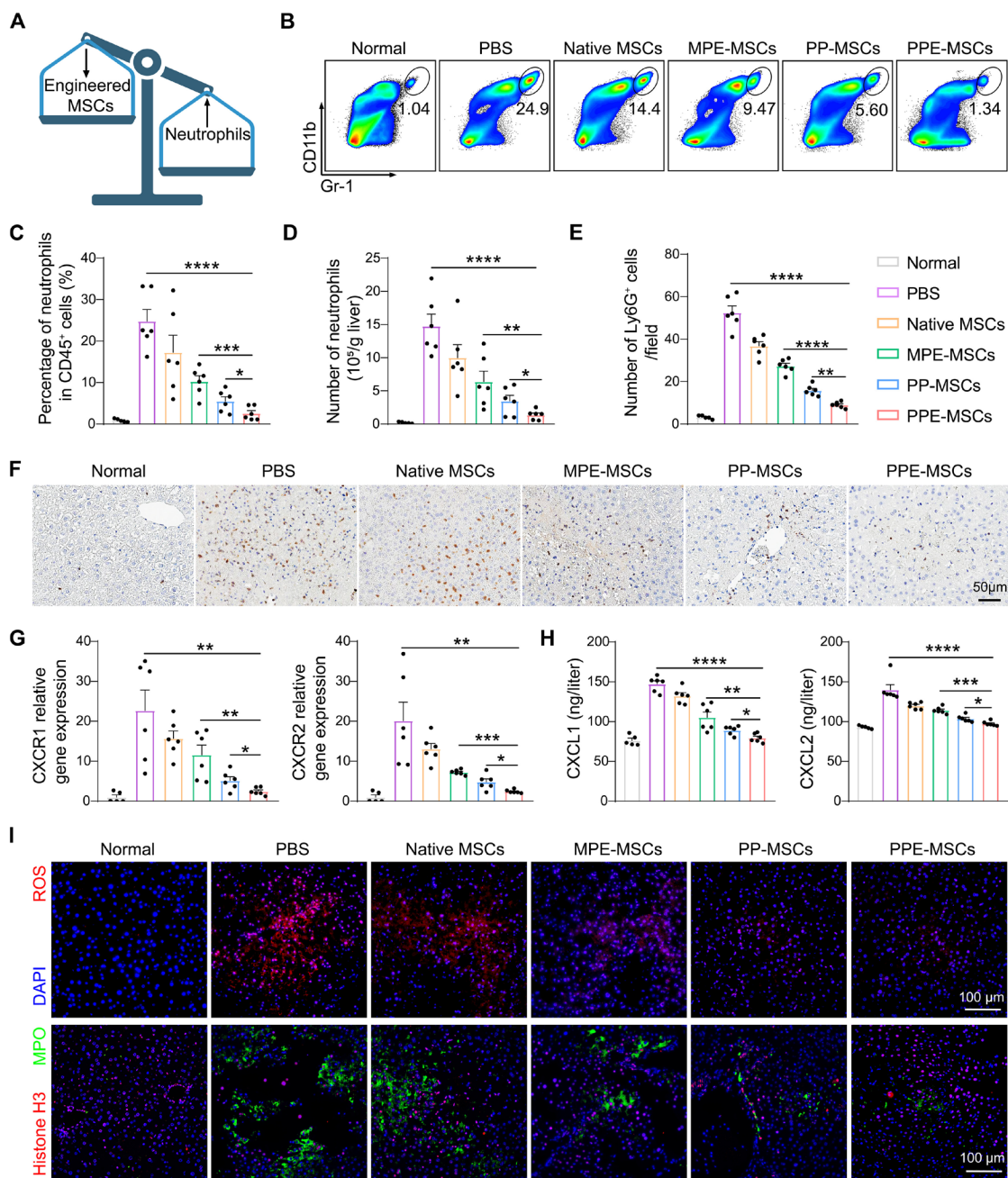
Fig. 3. Antagonistic effect of engineered MSCs on neutrophil infiltration into injured liver tissue. (**A**) Schematic illustration showing enhanced MSC targeting reduces neutrophil infiltration. (**B** to **D**) Flow cytometry analysis of neutrophil levels in liver tissue posttreatment. (B) Representative flow cytometry images showing neutrophil frequencies within the CD45+ cell population. (C) Statistical analysis of neutrophil percentages. (D) Quantification of intrahepatic neutrophil numbers per gram of liver tissue. Means ± SEM. $n = 6$ mice. (**E** and **F**) Representative immunohistochemistry images (F) and quantitative analysis (E) of Ly6G+ cells in the damaged liver tissue following various treatments. Representative images out of six images obtained are shown. Means ± SEM. $n = 6$ mice. (**G**) Real-time PCR results showing intrahepatic relative mRNA expression levels of CXCR1 and CXCR2. Means ± SEM. $n = 6$ mice. (**H**) Concentrations of CXCL1 and CXCL2 in the peripheral blood of ALF mice following various treatments. Means ± SEM. $n = 6$ mice. (**I**) Representative images showing ROS levels and NETs in liver tissues from ALF mice in different treatment groups. Representative images out of seven images obtained are shown. MPE-MSCs, monovalent P-selectin and E-selectin binding peptide-engineered MSCs; PP-MSCs, polyvalent P-selectin peptide-engineered MSCs; PPE-MSCs: polyvalent P-selectin and E-selectin binding peptide-engineered MSCs. For (C), (D), (E), (G), and (H), statistical analysis was performed by one-way ANOVA with Tukey's multiple comparisons tests (*$P < 0.05$; **$P < 0.01$; ***$P < 0.001$; ****$P < 0.0001$).
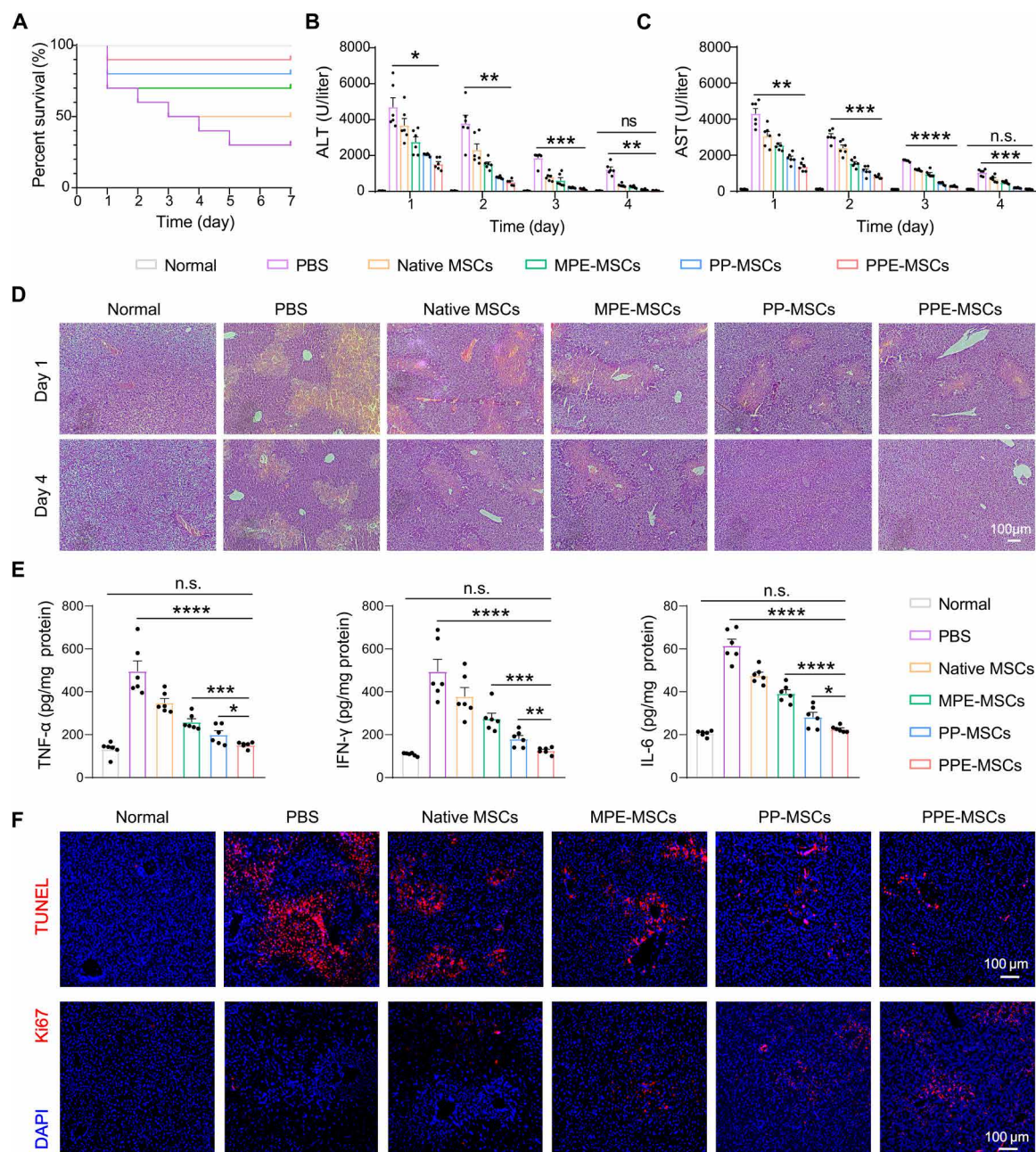
Fig. 4. Therapeutic efficacy of engineered MSCs in ALF mice. (**A**) Survival rates of ALF mice following various treatments. $n = 10$ mice. C57 mice were induced with ALF via intraperitoneal administration of APAP (500 mg/kg), followed by tail vein injections of either PBS or engineered MSCs. (**B** and **C**) Quantitative analysis of hematological markers of liver damage over 4 days. Means ± SEM. $n = 6$ mice. (**D**) H&E staining of liver tissues from ALF mice with different treatments. Representative images out of six images obtained are shown. (**E**) Levels of TNF-α, IFN-γ, and IL-6 in liver tissues after different treatments. Means ± SEM. $n = 6$ mice. (**F**) Immunofluorescence staining to analyze TUNEL-positive cells (red) and Ki67-positive cells (red) in ALF mouse livers following various treatments. Representative images out of six images obtained are shown. For (B) and (C), statistical analysis was performed by two-way ANOVA with Tukey's multiple comparisons tests. MPE-MSCs, monovalent P-selectin and E-selectin binding peptide-engineered MSCs; PP-MSCs, polyvalent P-selectin peptide-engineered MSCs; PPE-MSCs, polyvalent P-selectin and E-selectin binding peptide-engineered MSCs. For (F), statistical analysis was performed by one-way ANOVA with Tukey's multiple comparisons tests (*$P < 0.05$; **$P < 0.01$; ***$P < 0.001$; ****$P < 0.0001$; n.s., not significant).

PPE-MSCs group decreased by two-thirds on day 1 posttreatment and continued to decrease over time. By day 4, ALT and AST levels in the PPE-MSCs group were essentially identical to those in the normal group, whereas levels in the other groups were still above normal, highlighting the powerful therapeutic efficacy of PPE-MSCs in treating damaged livers. The process of liver tissue repair involves changes in tissue morphology. Therefore, we performed H&E staining of liver sections on day 1 and day 4 to assess tissue repair. The results showed that liver damage in the PPE-MSCs group was notably reduced compared to the other groups after 1 day of treatment (Fig. 4D). This effect was primarily attributed to the effective antagonism of neutrophil infiltration and subsequent alleviation of tissue damage by PPE-MSCs. By day 4, the PPE-MSCs group showed minimal tissue damage, almost comparable to the healthy control group, suggesting that PPE-MSCs alleviate damage caused by excessive neutrophil infiltration and promote tissue repair.

Moreover, we investigated the role of engineered MSCs in suppressing inflammation in liver tissue. On day 4, we extracted liver tissues to measure the levels of the inflammatory factors TNF-α, interferon-γ (IFN-γ), and IL-6. ELISA results revealed that the levels of pro-inflammatory factors in the liver tissue of mice treated with PPE-MSCs were almost the same as those in the normal group, indicating the excellent anti-inflammatory effects of PPE-MSCs (Fig. 4E). In addition, we corroborated the effects of engineered MSCs on the protection and proliferation of hepatocytes through immunofluorescence staining of liver (Fig. 4F and fig. S20). The number of terminal deoxynucleotidyl transferase–mediated deoxyuridine triphosphate nick end labeling (TUNEL)–positive apoptotic cells in the liver tissue of mice treated with PPE-MSCs was notably reduced, indicating the effective protective effect of PPE-MSCs on hepatocytes. Slow liver regeneration is a prominent characteristic of liver failure, and enhancing the proliferation capacity of hepatocytes is beneficial for its treatment (34). Ki-67 staining revealed that PPE-MSCs treatment fostered hepatocyte proliferation to a greater extent compared to other groups. In summary, PPE-MSCs effectively alleviate liver damage induced by excessive neutrophil infiltration, reduce mortality, and exhibit anti-inflammatory, anti-apoptotic, and pro-proliferation effects in treating damaged liver tissue. The strategy of engineering MSCs with bispecific polyvalent peptides demonstrated superior therapeutic effects in ALF mice.

To investigate the regulatory effects of PPE-MSCs on the immune microenvironment of the injured liver, we assessed immune cell populations in liver tissue. ALF mice were injected with PBS, native MSCs, or PPE-MSCs, and the immune cells in the liver were analyzed 4 days postinjection. T-distributed stochastic neighbor embedding (t-SNE) analysis visually depicted the distribution of myeloid cells and lymphocytes within the liver tissue (Fig. 5A and fig. S21). We observed pronounced changes in myeloid cells within the PPE-MSCs group compared to the untreated group. The average neutrophil percentage in the PPE-MSCs group was 0.4%, which did not significantly differ from the normal group (fig. S22). Monocytes constituted 32.3% of CD45$^+$ cells in the PBS group; following MSC treatment, this proportion substantially decreased to 13.1% in the native MSCs group and 6.5% in the PPE-MSCs group, approaching the levels observed in the normal group (6.0%) (Fig. 5B). Similarly, the proportion of F4/80$^+$ macrophages rose to 44.5% in the PBS group but substantially decreased to 16.5% in the PPE-MSCs group. Among F4/80$^+$ macrophages, the proportion of anti-inflammatory

M2 macrophages in the PPE-MSCs group was 12.5%, which was more than four times higher than that in the PBS group (3.0%) (Fig. 5C). In addition, studies have indicated that MSCs can modulate immunity in injured tissues by influencing the population of regulatory T (T$_{reg}$) cells. Therefore, we investigated the proportion of T$_{reg}$ cells in liver tissue of ALF mice. Our findings revealed a substantial increase in T$_{reg}$ cells in the PPE-MSCs group compared to the other groups (Fig. 5D). These results underscored the ability of PPE-MSCs to effectively improve the immune microenvironment of injured liver tissue through immune modulation.

Single-cell transcriptomic profiling of ALF mouse livers after PPE-MSCs treatment

Treatment with engineered MSCs reshapes the immune microenvironment of the damaged liver, especially the composition of myeloid cells. To elucidate the underlying mechanisms of engineered MSCs at the transcriptomic level, we conducted droplet-based scRNA-seq on liver tissues from ALF mice treated with PBS, native MSCs, and PPE-MSCs (Fig. 6A). After excluding certain cells and imposing a limit on the percentage of mitochondrial genes to ensure sample reliability (fig. S23A), we obtained 26,483 cells of three samples and identified 32 clusters for subsequent analysis (fig. S23B). These clusters were further categorized into 11 major cell types based on classical markers and specific transcriptional features (Fig. 6B). The heat map illustrates the correlation between cell clusters and their annotated cell types (fig. S23C), and the violin plot depicts the expression levels of marker genes across different cell types (fig. S23D).

The distribution of cell clusters in the liver revealed higher percentages of monocytes and neutrophils in the PBS group compared to the PPE-MSCs group, consistent with previous flow cytometry results. In contrast, the percentages of hepatocytes and endothelial cells were higher in the PPE-MSCs group, suggesting that PPE-MSCs have a more potent effect in repairing liver tissue (Fig. 6C). Hepatocytes constitute the primary cell type in liver tissue (35). To better understand the role of PPE-MSCs in promoting hepatocyte regeneration, we examined differentially expressed genes (DEGs) in hepatocytes between the PPE-MSCs group and the PBS group. Compared to the PBS group, hepatocytes in the PPE-MSCs group exhibited 816 up-regulated genes and 1132 down-regulated genes (fig. S24A). Specifically, the up-regulated genes in PPE-MSCs group hepatocytes were enriched for mitochondrial energy metabolic functions such as fatty acid degradation and oxidative phosphorylation pathways, as well as drug metabolism functions such as metabolism of xenobiotics by cytochrome P450 pathways (Fig. 6D). Conversely, pathways related to cell apoptosis, such as the P53 signaling pathway, were down-regulated (fig. S24B). These results suggest that PPE-MSCs treatment can restore mitochondrial function in hepatocytes and inhibit hepatocyte apoptosis. The comparison between the PPE-MSCs and Native MSCs groups also revealed an up-regulation of mitochondrial energy metabolism-related genes and a down-regulation of apoptosis-related genes in the PPE-MSCs group (fig. S24C), indicating that PPE modification substantial enhances the tissue repair capacity of MSCs. These findings from scRNA-seq analysis are further supported by in vitro experiments, demonstrating that PPE-MSCs protect hepatocyte mitochondria, reduce ROS production, and inhibit hepatocyte apoptosis under APAP-induced conditions (fig. S25). We further compared liver tissue from the PPE-MSCs group with that of the healthy group using scRNA-seq analysis. The results showed that the composition and function of the repaired liver in the PPE-MSCs group closely resembled that of the
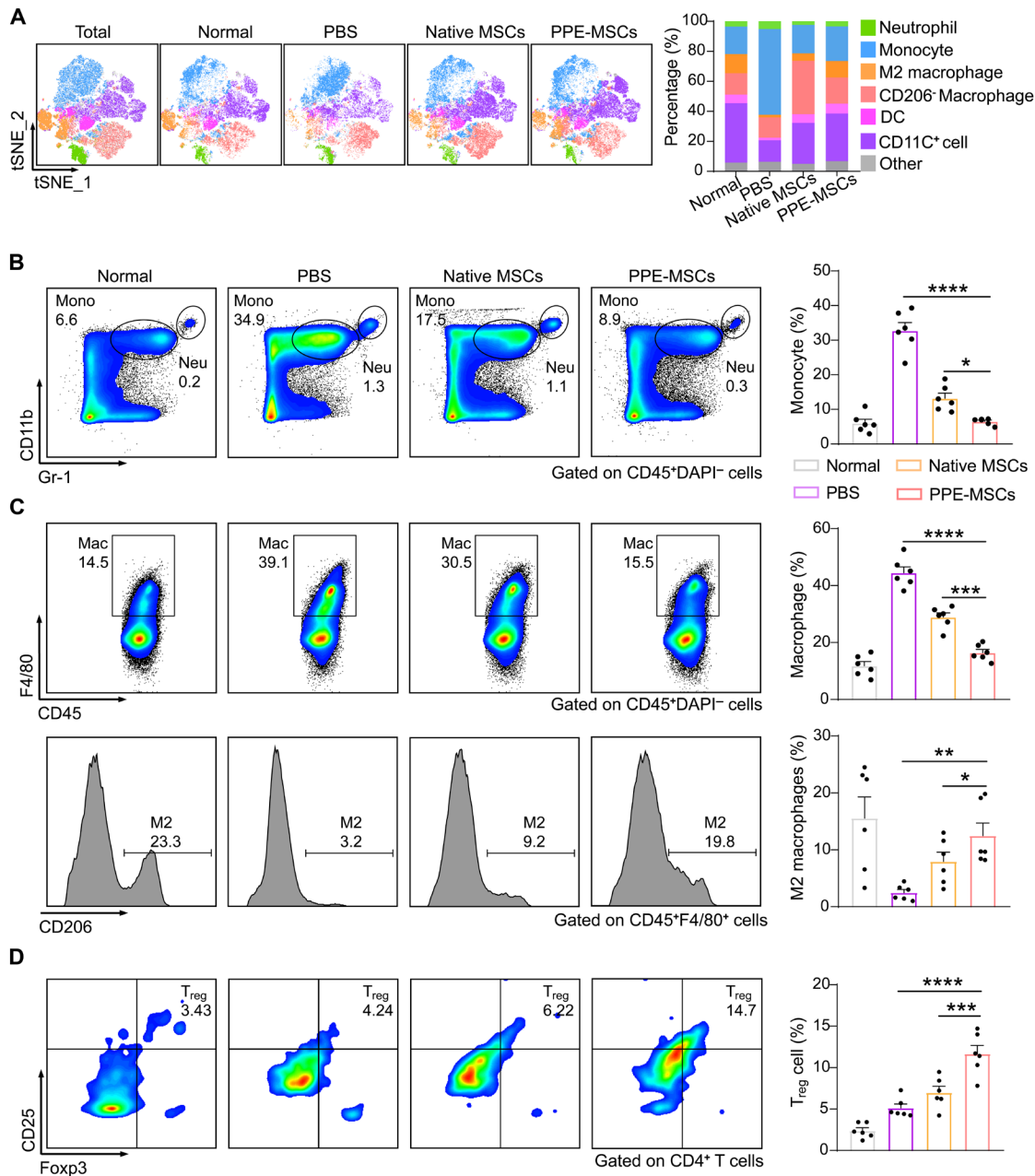
Fig. 5. Regulatory effects of engineered MSCs on the liver immune microenvironment in ALF mice. (**A**) T-SNE analysis of key myeloid cell subsets in the mouse liver based on multiparameter flow cytometry data. The left panel shows representative t-SNE plots, and the right panel displays corresponding percentage quantification. Colors representing different cell subsets defined by respective phenotypic markers, including neutrophils (CD11b$^+$ Ly6G$^+$), monocytes (CD11b$^+$ Ly6C$^+$), CD206$^-$ macrophages (CD11b$^+$ F4/80$^+$ CD206$^-$), M2 macrophages (F4/80$^+$ CD206$^+$), dendritic cells (DCs, CD11c$^+$ MHCII$^+$), CD11c$^+$ cells, and other cells. (**B**) Flow cytometry analysis showing representative dot plots of monocytes and neutrophils within CD45$^+$ cells (left), along with statistical data on monocyte percentages (right) in livers. (**C**) Flow cytometry analysis and quantification of total macrophages within CD45$^+$ cells (top) and M2 macrophages within the total macrophage population (bottom). (**D**) Flow cytometry analysis and quantification of T$_{reg}$ cells (CD25$^+$ Foxp3$^+$) within CD4$^+$ cells. PPE-MSCs, polyvalent P-selectin and E-selectin binding peptide-engineered MSCs. For (B), (C), and (D), means ± SEM, $n = 6$ mice. Statistical analysis was performed by one-way ANOVA with Tukey's multiple comparisons tests (*$P < 0.05$; **$P < 0.01$; ***$P < 0.001$; ****$P < 0.0001$).

healthy liver, underscoring the beneficial effects of PPE-MSCs on liver repair (fig. S26, A to E). Moreover, no significant differences were observed in the apoptotic pathways of Mono/Mac and neutrophils between the PPE-MSCs and healthy groups (fig. S26, F and G), suggesting that PPE-MSCs exert their effects by inhibiting neutrophil infiltration rather than influencing their survival.

Previous analysis of the immune microenvironment in damaged livers directed our attention to the monocyte/macrophage subset within liver tissue. Using marker gene expression levels, we performed additional unsupervised clustering of this subset, identifying six distinct clusters (Fig. 6E and fig. S27, A and B). Among these clusters, we identified a unique subgroup of macrophages
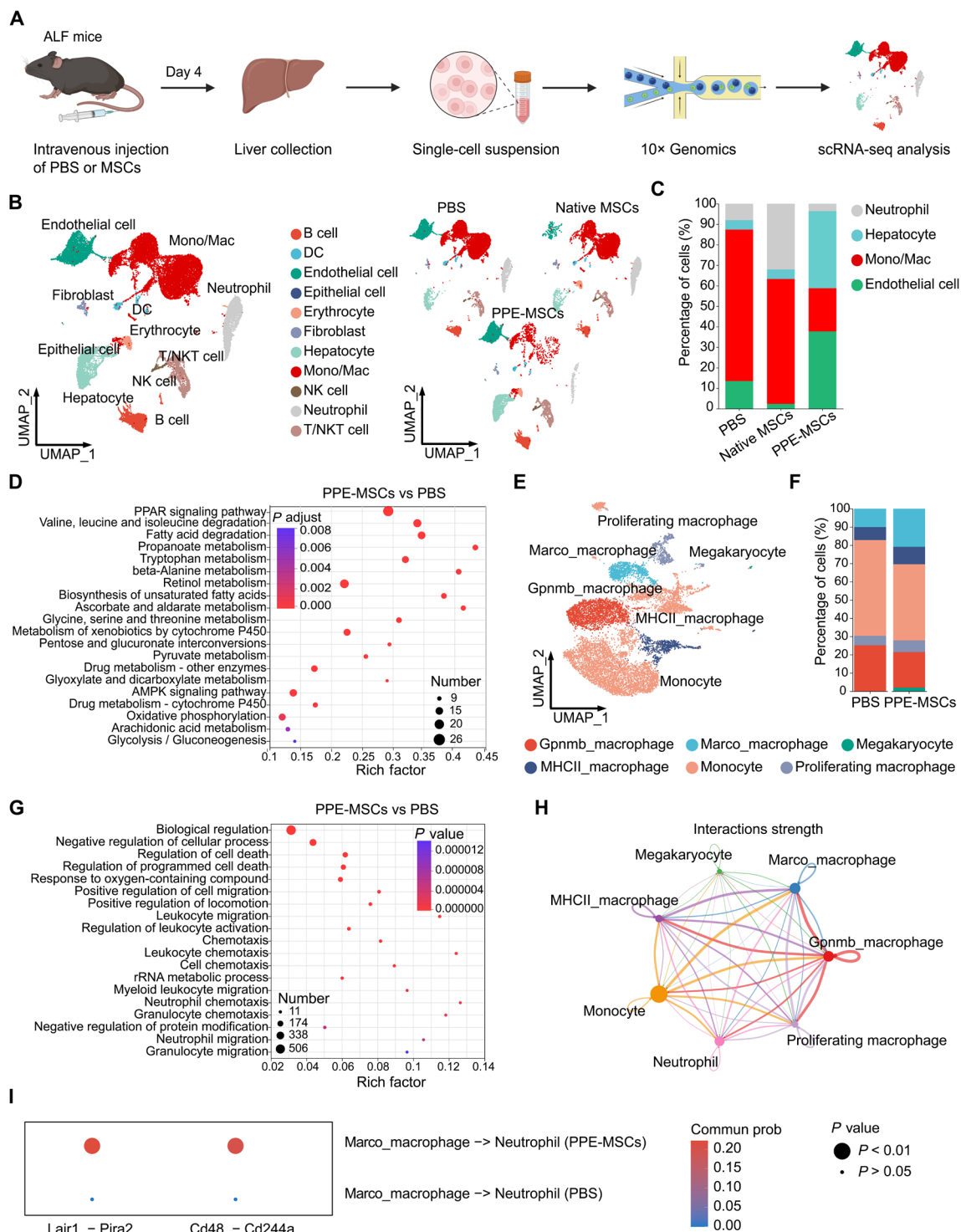
Fig. 6. ScRNA-seq analysis of livers in ALF mice with different treatments. (A) Schematic outlining the scRNA-seq procedure on ALF mouse liver using 10× Genomics. (**B**) UMAP plot of all intrahepatic cells showing 11 clusters (left). UMAP plots showing the distribution of intrahepatic cells from mice in different groups (right). (**C**) Relative changes in the cell ratios of neutrophil, hepatocyte, Mono/Mac, endothelial cell across the PBS, Native MSCs, and PPE-MSCs groups. (**D**) KEGG pathway analysis of differentially up-regulated genes in hepatocytes between the PPE-MSCs group and the PBS group. (**E**) UMAP visualization of monocyte/macrophage clusters. (**F**) Relative changes in the cell ratios of macrophages and monocytes across the PBS group and PPE-MSCs group. (**G**) GO pathway analysis of differentially down-regulated genes in Marco_macrophage between the PPE-MSCs group and the PBS group. (**H**) Cell-cell communication analysis illustrating the interaction strength between each pair of identified cell types within the PPE-MSCs group. (**I**) Bubble plot illustrating the expression levels of ligand-receptor pairs Lair1-Pira2 and Cd48-Cd244a across various cell types in both the PBS and PPE-MSCs groups. PPE-MSCs, polyvalent P-selectin and E-selectin binding peptide-engineered MSCs. The P values in (D), (G), and (I) were computed from one-sided permutation test.

termed Marco_macrophage. Trajectory analysis predicted that Marco_macrophages was a terminally differentiated cluster (fig. S27C). A previous study has shown that Marco_macrophage in the vicinity of the hepatic portal vein exhibit anti-inflammatory properties and express factors such as Il1rn and Tgfb1 that inhibit neutrophil hyperaggregation (fig. S27D) (36). We observed a notable increase in the proportion of Marco_macrophages in the livers of mice treated with PPE-MSCs (Fig. 6F) and found that gene sets associated with neutrophil chemotaxis and migration were downregulated in Marco_macrophages via Gene Ontology (GO) analysis (Fig. 6G). This suggests that PPE-MSCs effectively regulate the immune response by modulating both the quantity and function of Marco_macrophages.

Subsequently, we explored the landscape of cell-cell communication between different cell types. Initially, we inferred the number and strength of interactions between various cell populations and compared them across groups (Fig. 6H). Our analysis revealed that Marco_macrophages in the PPE-MSCs group exhibited enhanced interaction strength with neutrophils (fig. S27E). Further investigation into the ligand-receptor pairs involved in major cell cross-talk, depicted in a bubble plot, highlighted a more robust interaction network between Marco_macrophages and neutrophils in the PPE-MSCs group, particularly involving the Lair1-Pira2 and Cd48-Cd244a signaling pathways (Fig. 6I). These pathways are known to mediate immune cell interactions and signaling cascades (37, 38). In vitro experiments confirmed that blocking these two signaling pathways substantially reduced Marco$^+$ macrophages-mediated inhibition of activated neutrophils, underscoring the pivotal role of these pathways in the suppression of neutrophil activation by Marco$^+$ macrophages (fig. S28). We also observed that, compared to the PBS group, Marco_macrophages in the PPE-MSCs group reduced both the number and strength of interactions with monocytes. Analysis of ligand-receptor interactions indicated that PPE-MSCs attenuating Ccl6-Ccr2 signaling axis, thereby diminishing the interaction between Marco_macrophages and monocytes (fig. S29). In summary, PPE-MSCs enhance the inhibitory effect of Marco_macrophages on neutrophil chemotaxis and migration through the Lair1-Pira2 and Cd48-Cd244a signaling pathways, thereby reducing tissue damage and regulating inflammation.

DISCUSSION

Engineering MSCs using nongenetic methods has shown promise in improving therapeutic outcomes (39–41). Previous efforts have used selectin-binding peptides to enhance MSC homing efficiency, but these strategies were limited by the low binding affinity of the peptides (42, 43). The lack of multivalent peptide structures and the omission of synergistic effects from multiple selectin ligands led to only modest improvements in MSC adhesion. Our findings demonstrate that assembling peptides into polyvalent structures substantially increases their binding affinity, achieving levels comparable to native PSGL-1 binding to selectins. This enhancement broadens the potential applications for peptides and boosts their efficacy. Moreover, bispecific polyvalent peptides, composed of two distinct peptides, outperformed monospecific counterparts in mediating MSC adhesion. This superiority is likely due to the synergistic effects of the different functional domains within the bispecific structure, where each peptide separately influences the rolling flux and rolling velocity of cells on activated endothelial cells. Further research should explore the relationship between polypeptide structure and functional activity to identify which type of peptide can better trigger synergistic effects. In summary, bispecific polyvalent peptides offer a powerful tool for MSC engineering (44).

Neutrophil infiltration is often seen as a "double-edged sword" (45). As first responders to inflammation, neutrophils play a crucial role in clearing pathogens and cell debris, thereby promoting tissue repair. However, excessive neutrophil infiltration can lead to the release of pro-inflammatory factors and ROS, exacerbating tissue inflammation and damage (46, 47). Balancing neutrophil activity is essential for controlling inflammation and immune responses, making the regulation of excessive neutrophil infiltration a critical therapeutic strategy (2). Although the immunoregulatory effects of MSCs on neutrophils are well researched (48, 49), there is limited research on their ability to counteract excessive neutrophil infiltration. Ex vivo expanded MSCs often exhibit poor inhibitory effects on neutrophil infiltration, potentially due to their low homing efficiency. Our study reveals that engineering MSCs with polyvalent peptides substantially enhances their ability to inhibit neutrophil infiltration. The bispecific polyvalent peptide, with an affinity comparable to natural PSGL-1, boosts MSC homing efficiency, enabling them to compete with chemotactic neutrophils for selectin binding sites on endothelial cells. This finding highlights the potential of cell surface modification. Using appropriate biomolecules to engineer MSCs may lead to unexpectedly effective therapeutic outcomes.

APAP is widely used as an analgesic and antipyretic, but at high doses, it can cause severe liver necrosis, leading to ALF. APAP poisoning accounts for nearly half of all liver failure cases in the US and UK (50). ALF is a life-threatening condition marked by acute inflammation and severe liver dysfunction, with high mortality rates. Although liver transplantation is an effective treatment, it is limited by donor shortages and high treatment costs (51). MSC transplantation offers a promising alternative (52). In this study, we investigated the therapeutic effects of engineered MSCs on APAP-induced ALF. We found that within 24 hours of infusion, engineered MSCs effectively homed to the damaged liver and substantially inhibited excessive neutrophil infiltration. Once in the damaged tissue, MSCs themselves exerted immunomodulatory, anti-inflammatory, and anti-apoptotic effects. The combination of inhibiting excessive neutrophil infiltration and the intrinsic properties of MSCs resulted in superior therapeutic outcomes in ALF mice. scRNA-seq analysis of liver tissue revealed an increased proportion of Marco_macrophage following PPE-MSCs treatment. These cells exhibit anti-inflammatory and neutrophil-inhibitory characteristics. Future investigations should focus on elucidating the molecular pathways and cytokine profiles driving the differentiation or activation of these unique macrophages.

In summary, by using DNA template–directed molecular assembly, we constructed bispecific polyvalent peptides on the MSC surface. This cell surface engineering substantially enhanced MSC targeting and adhesion capabilities, as well as their ability to counteract excessive neutrophil infiltration. In addition, bispecific polyvalent peptides can be successfully assembled onto the surface of hMSCs, enhancing their targeting ability and effectively counteracting neutrophil infiltration. The engineered MSCs demonstrated superior therapeutic effects on damaged tissues and hold substantial potential for clinical applications.

MATERIALS AND METHODS

Materials
Oligonucleotides (table S1) were synthesized by Sangon Biotech Co. Ltd. (Shanghai, China). Peptides were synthesized by GL Biochem Ltd. NHS-PEG$_4$-DBCO cross-linker was purchased from Xi'an Confluore Biological Technology Co., Ltd. (catalog: BCD-7). SDS-PAGE Preparation Kit was obtained from Sangon Biotech Co. Ltd. (Shanghai, China). Cell Counting Kit-8, DiO/DiD cell-labeling solution, and Live/Dead viability/cytotoxicity kit were purchased from Beyotime Biotechnology Co. Ltd. (Shanghai, China). Dulbecco's modified Eagle's medium (DMEM) (high glucose and low glucose), RPMI 1640, trypsin-EDTA, and penicillin-streptomycin were procured from Gibco (Life Technologies, Carlsbad, CA, USA). Fetal bovine serum (FBS) was obtained from Biological Industries (catalog: 04-001ACS). The relevant information of flow cytometry antibodies is in table S4.

Animal treatments
Female BALB/c mice and Male C57BL/6 mice were purchased from Hunan SJA Laboratory Animal Co. Ltd. and housed in designated specific pathogen–free (SPF) animal facilities. All mice maintained under controlled conditions with a 12-hour/12-hour light/dark cycle, a temperature of 22°C, and humidity levels ranging from 45 to 60%.

Ethical statement
All mice were treated according to the standards in the Guide for the Care and Use of Laboratory Animals. All animal procedures were approved by the South China University of Technology Animal Care and Use Committee (2022020).

Cell culture
HUVECs [American Type Culture Collection (ATCC), PCS-100-013] were cultured in DMEM high glucose medium containing 10% FBS, supplemented with 1% penicillin and 1% streptomycin. HL-60 cells (ATCC, CCL-240) were cultured in RPMI 1640 medium containing 10% FBS, supplemented with 1% penicillin and 1% streptomycin. AML12 cells (iCell-m003, iCell Bioscience Inc., Shanghai, China) were cultured in DMEM/F-12 medium supplemented with 1% insulin-transferrin-selenium, dexamethasone (40 ng/ml), and 1% Gluta-MAX. The primary bone marrow MSCs from both mouse and human sources were procured from Shanghai Jinyuan Biotechnology Co. Ltd. were cultured in DMEM low glucose medium supplemented with 10% FBS, 1% penicillin, and 1% streptomycin. All cells were maintained at 37°C in a 5% CO$_2$ incubator with 95% relative humidity. Experiments were conducted using MSCs from passages 3 to 6.

Preparation of DNA-peptides
To prepare DNA-DBCO, synthesized DNA-NH$_2$ is fully dissolved in 100 μl of PBS containing 50 mM NaHCO$_3$ at a concentration of 100 μM. Next, 3 μl of 30 mM NHS-PEG$_4$-DBCO is added, and the reaction is allowed to proceed for 4 hours. After this period, an additional 3 μl of 30 mM NHS-PEG$_4$-DBCO is added, and the reaction continues for another 4 hours. Following the completion of the reaction, purification is performed using an Amicon 10 kDa MWCO centrifugal filter. For peptide preparation, the peptide is completely dissolved in anhydrous DMSO (dimethyl sulfoxide) to achieve a concentration of 2 mM. Then, 2 μl of this peptide solution is added to the 100 μM DNA-DBCO mixture, and the reaction is conducted at 37°C for 12 hours. Postreaction purification is performed using an Amicon 10 kDa MWCO centrifugal filter.

Surface engineering of MSCs
A total of 1×10^6 MSCs were suspended in 1 ml of PBS and centrifuged at 300g for 5 min. The supernatant was discarded, and the cells were washed once more with PBS before being resuspended in 200 μl of PBS. A DI-cholesterol solution was added to achieve a final concentration of 1 μM. The mixture was incubated with the cells in a 600 rpm oscillating metal bath for 20 min to facilitate the immobilization of DI on the cell surface. After incubation, the cells were washed twice with 1 ml of PBS to remove excess DI-cholesterol and then resuspended in 200 μl of PBS. For monovalent cell engineering, DM1-PBP and DM1-EBP peptides were added to the cell suspension to a final concentration of 1 μM each. For polyvalent cell engineering, DM1-PBP and DM2-EBP peptides were used, also at a final concentration of 1 μM each.

Quantitation of DI on the cell surface
To quantify the amount of DI on cell surface, MSCs (2×10^6) were suspended in PBS containing varying concentrations of DI-cholesterol (ranging from 0.05 to 2 μM) and incubated at room temperature (RT) for 20 min. The cells were then washed three times with PBS and exposed to fluorescently labeled complementary sequence (0.05 to 2 μM) before being incubated at RT for an additional hour. Following further washes, the cells were lysed using RIPA lysis buffer (Sangon, C500005-0100), and fluorescence intensity was measured with a fluorescence spectrophotometer. Last, the fluorescence data were fitted to a standard curve to quantify the number of DI molecules present on the cell surface.

The proliferation and paracrine of engineered MSCs
For proliferation analysis, engineered MSCs were seeded in a 96-well plate at a density of 3000 cells per well in 200 μl of complete medium. After 24 or 48 hours of culture, 10 μl of CCK-8 reagent was added to each well and incubated at 37°C for 1 hour. Absorbance was then measured at 450 nm using a microplate reader. Concurrently, cells seeded in a 24-well plate were stained using a Live/Dead Double Staining Kit, and fluorescence images were captured with a fluorescence microscope at the specified time points. For paracrine analysis, MSCs were plated in a 12-well plate at a density of 5×10^4 cells per well in complete medium for 24 hours to allow for cell adhesion. The medium was then replaced with a serum-free medium, and the cells were incubated for an additional 3 days. The supernatant was collected by centrifugation (3000 rpm for 20 min) and analyzed using ELISA kits according to the manufacturer's instructions (Shanghai Enzyme-linked Biotechnology Co. Ltd.).

Adhesion and antagonistic assay
HUVECs were cultured in 12-well plates and pretreated with TNF-α (10 ng/ml) for 6 hours. For adhesion experiments, MSCs were first stained with 1 μM Calcein AM and then subjected to engineering modification with DNA-peptides. The culture medium of HUVECs was aspirated and rinsed once with PBS. Subsequently, 1×10^5 native or engineered MSCs were resuspended in 1 ml of PBS and added to the HUVECs. After incubating at RT for 1 hour, the suspension was aspirated, and the cells were rinsed three times with 1 ml of PBS. For antagonistic experiments, engineered MSCs were added to HUVECs for adhesion, followed by the addition of HL-60 cells stained with 10 μM CellTrace Red CMTPX (Yeasen Biotechnology Co. Ltd., 40717ES50). After incubating at RT for 1 hour, the suspension was aspirated, and the cells were rinsed three times with 1 ml of PBS. Cellular imaging was performed using a Nikon fluorescence microscope immediately,

and ImageJ software was used to quantify the number of adherent cells by counting green (Calcein AM-stained MSCs) and red (Cell-Trace Red CMTPX-stained HL-60 cells) fluorescent cells.

Biosafety analysis in vivo

Six-week-old female BALB/c mice were used for in vivo biosafety testing. The mice were randomly divided into five groups: untreated, native MSCs, MPE-MSCs, PP-MSCs, and PPE-MSCs. Each group received the corresponding treatment. After 48 hours, the mice were euthanized, and whole blood and spleens were collected for analysis. For blood collection, peripheral blood was obtained via orbital bleeding using heparinized tubes. Blood cells were separated by centrifugation at $400g$ for 5 min at 4°C. The supernatant (serum) was further centrifuged at $2000g$ for 20 min at 4°C to prepare it for serological evaluation. The collected cells were resuspended in 10 ml of red blood cell lysis buffer, incubated at 4°C for 10 min, and then neutralized with 10 ml of $1 \times$ PBS. After centrifugation at $400g$ for 5 min at 4°C, the cells were collected. For splenocyte collection, spleens were removed and gently ground using the rough surface of a slide. The ground tissue was filtered through a 200-mesh nylon mesh into a 15-ml centrifuge tube, and cells were collected by centrifugation at $400g$ for 5 min. The cells were treated with 2 ml of red blood cell lysis buffer, incubated at 4°C for 10 min, and then neutralized with 10 ml of $1 \times$ PBS. After centrifugation at $400g$ for 5 min, the cells were collected. Both blood cells and splenocytes were stained with antibodies and analyzed using flow cytometry for further evaluation.

Experiment on acute inflammation of mouse ears

The dermal inflammation model induced by LPS in the mouse pinna was established following established protocols. Female BALB/c mice aged 6 to 8 weeks, with an average body weight of 19 to 20 g, were used. Mice were administered 30 μg of LPS (Sigma-Aldrich, L6529) in 30 μl of saline injected into the posterior/dorsal dermis of the right ear, whereas the contralateral ear received an injection of 0.9% saline as a control. Six hours post LPS injection, 1×10^6 native or engineered MSCs, pretreated with Vybrant-DiD staining buffer for tracking purposes, were intravenously administered in 150 μl of PBS. After 48 hours, the mice were euthanized, and the ears were collected for analysis. Fluorescence imaging of the ears was performed using IVIS Lumina Series III (PerkinElmer) immediately after ear collection, and image analysis and quantification of fluorescence intensity were conducted using Living Image 4.4 software. For frozen section and immunofluorescence staining, the ears were carefully removed, cleaned of most hair, and immediately frozen in liquid nitrogen. The ear tissue was embedded in optimal cutting temperature (OCT) compound (SAKURA) under low-temperature conditions and sliced using a freezing microtome (Leica, CM1950). Tissue slices were then immunofluorescently stained overnight with anti-CD31 antibody (BioLegend, 102506) to label blood vessels. DAPI (4′,6-diamidino-2-phenylindole) staining was performed to visualize cell nuclei. Last, the sections were examined under a fluorescence microscope.

APAP-induced ALF model in mice

APAP (Aladdin, A105809) was dissolved in physiological saline by heating at 50°C. Male C57BL/6 mice aged 6 to 8 weeks, with an average body weight of 22 to 24 g, were fasted for 16 hours with free access to water. Each mouse received an intraperitoneal injection of APAP (300 to 500 mg/kg), followed by resumption of normal diet intake postinjection. The mice were continuously monitored for their condition, and survival rates were recorded. Peripheral blood samples were collected at specified time points, and serum was obtained for testing ALT and AST levels using a HITACHI Automatic Analyzer. Mice were euthanized at the designated time points, and liver tissues were collected and processed into paraffin sections for H&E staining.

IVIS imaging of mouse liver

ALF was induced in mice by intraperitoneal injection of APAP (500 mg/kg). Engineered MSCs labeled with Vybrant-DiD were subsequently administered intravenously. Imaging was performed at 24 and 48 hours postinjection using IVIS in vivo imaging after depilation of the mice's abdomen and anesthesia induction with isoflurane.

Flow cytometry quantification of neutrophils in liver

After fully bleeding the mice, the liver was removed and weighed. It was then homogenized by grinding on a 200-mesh steel wire mesh until sufficiently homogenized. The resulting solution was transferred to a 15-ml centrifuge tube and centrifuged at $450g$ for 5 min to remove the supernatant. The precipitate was resuspended in 8 ml of 40% Percoll solution and centrifuged at $800g$ for 20 min. After discarding the impurities and the upper layer of Percoll, the cell pellet was resuspended in 2 ml of red blood cell lysis buffer in a clean 15-ml centrifuge tube. The suspension was incubated at 4°C for 10 min, followed by the addition of 10 ml of $1 \times$ PBS to stop the lysis reaction. The cells were then centrifuged at $450g$ for 5 min to collect them. The cell pellet was resuspended, and cell counting was performed. Last, the cells were stained with antibodies for flow cytometry analysis.

Biodistribution assay

Male C57BL/6 mice were intraperitoneally injected with APAP to induce ALF. MSCs were prestained with Vybrant-DiD for tracking purposes. Subsequently, the mice were intravenously injected with either PBS, 1×10^6 native MSCs, or engineered MSCs. After 24 hours, the mice were euthanized, and their hearts, livers, spleens, lungs, and kidneys were collected for fluorescence imaging using the IVIS Lumina Series III. The acquired images were analyzed, and fluorescence intensity was quantified using Living Image 4.4 software.

Immunohistochemistry staining

Formalin-fixed paraffin embedded liver tissue slides were dewaxed and rehydrated. After antigen retrieval, slides were blocked with goat serum at RT for 20 min. Primary antibody Ly6G (1:200 dilution, Cell Signaling Technology, 87048S) was incubated overnight at 4°C. Slides were washed and incubated with horseradish peroxidase–conjugated secondary antibody (Panovue, 0004100100) at RT for 10 min. 3,3′-Diaminobenzidine (DAB) (1:50 dilution, Abcam, ab64238) was used as substrate for staining. All the IHC staining slides were scanned using a Aperio CS2 scanner (Leica). Six independent fields were analyzed per liver section. Ly6G-positive cells were quantified by Image J.

H&E staining

Mouse liver tissue was fixed in 4% paraformaldehyde, dehydrated, paraffin-embedded, and sectioned into 4-μm-thick slices. These sections were subsequently stained with H&E to observe tissue damage under a microscope.

Flow cytometry to detect immune cells in liver tissue

Liver tissue was enzymatically digested to obtain single cells. Briefly, the tissue was minced and resuspended in RPMI 1640

supplemented with collagenase IV (1 mg/ml). After incubation on a shaker at 120 rpm for 15 min, the suspension was filtered through a 200-mesh nylon mesh to remove undigested tissue fragments. The cells were then collected by centrifugation at $300g$ for 5 min at 4°C. Following cell counting, the cells were stained with antibodies.

Flow cytometry and t-SNE analysis

Single-cell suspensions were preincubated with purified anti-mouse CD16/32 (BioLegend, 101301) to block Fc receptors and then stained with a cocktail of fluorochrome-conjugated antibodies for 20 min at 4°C. After surface marker staining, cells were fixed and permeabilized with the Foxp3/Transcription Factor Staining Buffer Set (eBioscience, 00-5523-00) for CD206 detection. The information of antibodies used was listed in table S4. Flow cytometry data were acquired on a Cytek Aurora spectral flow cytometer (Cytek Biosciences), and analyzed using FlowJo software (V10, BD Biosciences). T-SNE analysis of lymphocytes and myeloid cells from multiparameter flow cytometry data was performed using the t-SNE plug-in within FlowJo software.

Single-cell RNA sequencing

After 4 days of treatment, liver tissues from mice in different experimental groups (treated with PBS, native MSCs, or PPE-MSCs) were collected, digested, and subjected to scRNA-seq. Cell viability was assessed using trypan blue staining. The scRNA-seq library was constructed using the Single Cell 3' Reagent Kit v3.1 (10× Genomics) based on the manufacturer's protocol. The sequencing was sequenced on Novaseq Xplus using PE150 mode. Both sequencing and bioinformatics analyses were conducted by Majorbio Co. Ltd. (Shanghai, China).

scRNA-seq data quality control and preprocessing

Reads were processed using the Cell Ranger (version 7.1.0) pipeline with default and recommended parameters. FASTQs generated from Illumina sequencing output were aligned to the mouse genome, version GRCm39, using the STAR algorithm. Cell Ranger (version 7.1.0) with Seurat (version 4.1.1) was used to generate gene-barcode matrices for quality control and downstream analysis. Upon acquiring the matrices, we first excluded cells with fewer than 200 or more than 6000 unique genes. Only genes detected in 10 or more cells were included for further analysis. Cells with mitochondrial gene expression exceeding 10% were also discarded. After filtration, a total of 26,483 cells were applied for further analysis. Dimensionality reduction was performed using the Seurat R package (version 4.1.1). The gene expression matrices were normalized to the total unique molecular identifiers (UMI) counts per cell and transformed to the natural log scale. The 2000 most variable genes were selected using the FindVariableFeatures function in Seurat, and principal components analysis (PCA) was conducted based on these genes. For each cell type, the number of principal components (PCs) was chosen based on the knee point of the scree plot using the ElbowPlot function in Seurat, with the top 30 PCs retained for subsequent analysis. The FindNeighbors and RunUMAP functions were then applied, and cell clustering was performed using the FindClusters function with a resolution of 0.8. Last, two-dimensional UMAP was used to visualize the cell clusters. The scRNA-seq data have been deposited into the Gene Expression Omnibus (GEO) database under accession code GSE286317. Furthermore, normal control mouse liver scRNA-seq data were acquired from GSE228305. After the same filtering conditions, 14,677 cells were applied for further analysis.

Analysis of scRNA-seq data

DEGs between different samples or consecutive clusters were identified using the FindAllMarkers function implemented in Seurat. GO and Kyoto Encyclopedia of Genes and Genomes (KEGG) analysis were performed to identify biological functions or pathways that are significantly associated with the specifically expressed genes using R package clusterProfiler (version 4.6.2). Gene set enrichment Analysis (GSEA) was used for pathway analysis. Pseudotime trajectory analysis was performed using Monocle2 (version 2.22.0) to identify significant transformational relationships among cell types. Cell-cell communication analysis was conducted according to the ligand-receptor pairs among different cell types using CellChat (version 1.5.0).

In vitro validation experiments

Coculture of MSCs and hepatocytes. MSCs and AML12 cells were seeded in a 12-well plate at a specific ratio of MSCs to AML12 cells, with 1×10^5 cells of each type per well. After 12 hours of culture, APAP (20 mM) was added, and the cells were incubated for an additional 12 hours. After incubation, mitochondrial membrane potential and apoptosis in AML12 cells were assessed. The cells were stained using mitochondrial membrane potential and apoptosis detection kits (Beyotime Biotechnology Co. Ltd. C1071S), and then observed under a microscope. Coculture of Marco$^+$ macrophages and neutrophils. Marco$^+$ macrophages were isolated from healthy mice and seeded in a 12-well plate at a density of 1×10^5 cells per well. Neutrophils were extracted from the livers of ALF mice and added to each well at a density of 5×10^5 cells per well. To block specific signaling, anti-CD48 (10 µg/ml, BioLegend, 103405) and anti-Lair1 (10 µg/ml, Thermo Fisher Scientific, 16-3051-82) antibodies were dissolved in 1% serum DMEM and incubated with the Marco$^+$ macrophages at 37°C for 1 hour. The neutrophils were then cocultured with the treated Marco$^+$ macrophages. Cytokine levels in the supernatant, neutrophil-related mRNA expression, and ROS levels released by neutrophils were measured 24 hours post-coculture.

Statistical analysis

Data analyses were performed using GraphPad Prism8. Data were analyzed using the unpaired Student's t test, one-way, or two-way analysis of variance (ANOVA) to evaluate the statistical significance of group differences. $P < 0.05$ was considered to be statistically significant.

Supplementary Materials

This PDF file includes:
Figs. S1 to S29
Tables S1 to S4

REFERENCES AND NOTES

1. S. de Oliveira, E. E. Rosowski, A. Huttenlocher, Neutrophil migration in infection and wound repair: Going forward in reverse. *Nat. Rev. Immunol.* **16**, 378–391 (2016).
2. T. Nemeth, M. Sperandio, A. Mocsai, Neutrophils as emerging therapeutic targets. *Nat. Rev. Drug Discov.* **19**, 253–275 (2020).
3. K. Liu, F. S. Wang, R. Xu, Neutrophils in liver diseases: Pathogenesis and therapeutic targets. *Cell. Mol. Immunol.* **18**, 38–44 (2021).
4. G. Wigerblad, M. J. Kaplan, Neutrophil extracellular traps in systemic autoimmune and autoinflammatory diseases. *Nat. Rev. Immunol.* **23**, 274–288 (2023).
5. A. Herrero-Cervera, O. Soehnlein, E. Kenne, Neutrophils in chronic inflammatory diseases. *Cell. Mol. Immunol.* **19**, 177–191 (2022).
6. P. E. Marques, S. S. Amaral, D. A. Pires, L. L. Nogueira, F. M. Soriani, B. H. Lima, G. A. Lopes, R. C. Russo, T. V. Ávila, J. G. Melgaço, A. G. Oliveira, M. A. Pinto, C. X. Lima, A. M. De Paula, D. C. Cara, M. F. Leite, M. M. Teixeira, G. B. Menezes, Chemokines and mitochondrial

products activate neutrophils to amplify organ injury during mouse acute liver failure. *Hepatology* **56**, 1971–1982 (2012).

7. J. Woytschak, N. Keller, C. Krieg, D. Impellizzieri, R. W. Thompson, T. A. Wynn, A. S. Zinkernagel, O. Boyman, Type 2 interleukin-4 receptor signaling in neutrophils antagonizes their expansion and migration during infection and inflammation. *Immunity* **45**, 172–184 (2016).

8. E. Kolaczkowska, P. Kubes, Neutrophil recruitment and function in health and inflammation. *Nat. Rev. Immunol.* **13**, 159–175 (2013).

9. V. R. Krishnamurthy, M. Y. Sardar, Y. Ying, X. Song, C. Haller, E. Dai, X. Wang, D. Hanjaya-Putra, L. Sun, V. Morikis, S. I. Simon, R. J. Woods, R. D. Cummings, E. L. Chaikof, Glycopeptide analogues of PSGL-1 inhibit P-selectin in vitro and in vivo. *Nat. Commun.* **6**, 6387 (2015).

10. N. Milošević, M. Rütter, Y. Ventura, Y. Kezerle, V. Feinshtein, A. David, Attenuation of neutrophil-mediated liver injury in mice by drug-free E-selectin binding polymer. *J. Control. Release* **319**, 475–486 (2020).

11. H. K. Salem, C. Thiemermann, Mesenchymal stromal cells: Current understanding and clinical status. *Stem Cells* **28**, 585–596 (2010).

12. S. Lou, Y. Duan, H. Nie, X. Cui, J. Du, Y. Yao, Mesenchymal stem cells: Biological characteristics and application in disease therapy. *Biochimie* **185**, 9–21 (2021).

13. M. F. Pittenger, D. E. Discher, B. M. Peault, D. G. Phinney, J. M. Hare, A. I. Caplan, Mesenchymal stem cell perspective: Cell biology to clinical progress. *NPJ Regen. Med.* **4**, 22 (2019).

14. J. M. Karp, G. S. L. Teo, Mesenchymal stem cell homing: The devil is in the details. *Cell Stem Cell* **4**, 206–216 (2009).

15. M. Ullah, D. D. Liu, A. S. Thakor, Mesenchymal stromal cell homing: Mechanisms and strategies for improvement. *iScience* **15**, 421–438 (2019).

16. Y. Su, X. Lei, L. Wu, L. Liu, The role of endothelial cell adhesion molecules P-selectin, E-selectin and intercellular adhesion molecule-1 in leucocyte recruitment induced by exogenous methylglyoxal. *Immunology* **137**, 65–79 (2012).

17. R. P. McEver, Selectins: Initiators of leucocyte adhesion and signalling at the vascular wall. *Cardiovasc. Res.* **107**, 331–339 (2015).

18. M. Kabat, I. Bobkov, S. Kumar, M. Grumet, Trends in mesenchymal stem cell clinical trials 2004-2018: Is efficacy optimal in a narrow dose range? *Stem Cells Transl. Med.* **9**, 17–27 (2020).

19. P. Shi, X. Wang, B. Davis, J. Coyne, C. Dong, J. Reynolds, Y. Wang, In situ synthesis of an aptamer-based polyvalent antibody mimic on the cell surface for enhanced interactions between immune and cancer cells. *Angew. Chem. Int. Ed. Engl.* **59**, 11892–11897 (2020).

20. P. Shi, Y. Wang, Synthetic DNA for cell-surface engineering. *Angew. Chem. Int. Ed. Engl.* **60**, 11580–11591 (2021).

21. P. Shi, N. Zhao, J. Lai, J. Coyne, E. R. Gaddes, Y. Wang, Polyvalent display of biomolecules on live cells. *Angew. Chem. Int. Ed. Engl.* **57**, 6800–6804 (2018).

22. N. Chen, X. Shi, Y. Wang, Molecularly regulated reversible DNA polymerization. *Angew. Chem. Int. Ed. Engl.* **55**, 6657–6661 (2016).

23. T. K. Epperson, K. D. Patel, R. P. McEver, R. D. Cummings, Noncovalent association of P-selectin glycoprotein ligand-1 and minimal determinants for binding to P-selectin. *J. Biol. Chem.* **275**, 7839–7853 (2000).

24. A. Cugno, A. Marki, K. Ley, Biomechanics of neutrophil tethers. *Life* **11**, 515 (2021).

25. H. Wang, C. N. Alarcon, B. Liu, F. Watson, S. Searles, C. K. Lee, J. Keys, W. Pi, D. Allen, J. Lammerding, J. D. Bui, R. L. Klemke, Genetically engineered and enucleated human mesenchymal stromal cells for the targeted delivery of therapeutics to diseased tissue. *Nat. Biomed. Eng.* **6**, 882–897 (2022).

26. H. Wei, F. Li, T. Xue, H. Wang, E. Ju, M. Li, Y. Tao, MicroRNA-122-functionalized DNA tetrahedron stimulate hepatic differentiation of human mesenchymal stem cells for acute liver failure therapy. *Bioact. Mater.* **28**, 50–60 (2023).

27. M. Saleh, M. Taher, A. A. Sohrabpour, A. A. Vaezi, M. Nasiri Toosi, M. Kavianpour, Z. Ghazvinian, S. Abdolahi, J. Verdi, Perspective of placenta derived mesenchymal stem cells in acute liver failure. *Cell Biosci.* **10**, 71 (2020).

28. D. Y. Lee, B. H. Cha, M. Jung, A. S. Kim, D. A. Bull, Y. W. Won, Cell surface engineering and application in cell delivery to heart diseases. *J. Biol. Eng.* **12**, 28 (2018).

29. J. C. Mossanen, F. Tacke, Acetaminophen-induced acute liver injury in mice. *Lab. Anim* **49**, 30–36 (2015).

30. J. A. Hinson, D. W. Roberts, L. P. James, Mechanisms of acetaminophen-induced liver necrosis. *Handb. Exp. Pharmacol.* **196**, 369–405 (2010).

31. H. Jaeschke, C. D. Williams, A. Ramachandran, M. L. Bajt, Acetaminophen hepatotoxicity and repair: The role of sterile inflammation and innate immunity. *Liver Int.* **32**, 8–20 (2012).

32. S. Kumar, S. Ponnazhagan, Bone homing of mesenchymal stem cells by ectopic alpha 4 integrin expression. *FASEB J.* **21**, 3917–3927 (2007).

33. A. Capucetti, F. Albano, R. Bonecchi, Multiple roles for chemokines in neutrophil biology. *Front. Immunol.* **11**, 1259 (2020).

34. H. Wei, K. Yi, F. Li, D. Li, J. Yang, R. Shi, Y. Jin, H. Wang, J. Ding, Y. Tao, M. Li, Multimodal tetrahedral DNA nanoplatform for surprisingly rapid and significant treatment of acute liver failure. *Adv. Mater.* **36**, 2305826 (2024).

35. Z. Zhou, M. J. Xu, B. Gao, Hepatocytes: A key cell type for innate immunity. *Cell. Mol. Immunol.* **13**, 301–315 (2016).

36. Y. Miyamoto, J. Kikuta, T. Matsui, T. Hasegawa, K. Fujii, D. Okuzaki, Y. C. Liu, T. Yoshioka, S. Seno, D. Motooka, Y. Uchida, E. Yamashita, S. Kobayashi, H. Eguchi, E. Morii, K. Tryggvason, T. Shichita, H. Kayama, K. Atarashi, J. Kunisawa, K. Honda, K. Takeda, M. Ishii, Periportal macrophages protect against commensal-driven liver inflammation. *Nature* **629**, 901–909 (2024).

37. F. Van Laethem, L. Donaty, E. Tchernonog, V. Lacheretz-Szablewski, J. Russello, D. Buthiau, M. Almeras, J. Moreaux, C. Bret, LAIR1, an ITIM-Containing receptor involved in immune disorders and in hematological neoplasms. *Int. J. Mol. Sci.* **23**, 16136 (2022).

38. J. Liu, L. Xing, J. Li, K. Wen, N. Liu, Y. Liu, G. Wu, S. Wang, D. Ogiya, T. Y. Song, K. Kurata, J. Penailillo, E. Morelli, T. Wang, X. Hong, A. Gulla, Y. T. Tai, N. Munshi, P. Richardson, R. Carrasco, T. Hideshima, K. C. Anderson, Epigenetic regulation of CD38/CD48 by KDM6A mediates NK cell response in multiple myeloma. *Nat. Commun.* **15**, 1367 (2024).

39. T. Ye, X. Liu, X. Zhong, R. Yan, P. Shi, Nongenetic surface engineering of mesenchymal stromal cells with polyvalent antibodies to enhance targeting efficiency. *Nat. Commun.* **14**, 5806 (2023).

40. J. Park, B. Andrade, Y. Seo, M. J. Kim, S. C. Zimmerman, H. Kong, Engineering the surface of therapeutic "living" cells. *Chem. Rev.* **118**, 1664–1690 (2018).

41. R. Sackstein, J. S. Merzaban, D. W. Cain, N. M. Dagia, J. A. Spencer, C. P. Lin, R. Wohlgemuth, Ex vivo glycan engineering of CD44 programs human multipotent mesenchymal stromal cell trafficking to bone. *Nat. Med.* **14**, 181–187 (2008).

42. H. Yan, X. Mi, A. C. Midgley, X. Du, Z. Huang, T. Wei, R. Liu, T. Ma, D. Zhi, D. Zhu, T. Wang, G. Feng, Y. Zhao, W. Zhang, J. He, M. Zhu, D. Kong, K. Wang, Targeted repair of vascular injury by adipose-derived stem cells modified with P-selectin binding peptide. *Adv. Sci.* **7**, 1903516 (2020).

43. B. Huang, X. C. Jiang, T. Y. Zhang, Y. L. Hu, Y. Tabata, Z. Chen, S. Pluchino, J. Q. Gao, Peptide modified mesenchymal stem cells as targeting delivery system transfected with miR-133b for the treatment of cerebral ischemia. *Int. J. Pharm.* **531**, 90–100 (2017).

44. L. M. Iakoucheva, C. Diener, G. G. R. Martínez, D. M. Blas, D. A. C. González, G. Corzo, S. Castro-Obregon, G. Del Rio, Effective design of multifunctional peptides by combining compatible functions. *PLoS Comput. Biol.* **12**, e1004786 (2016).

45. M. Metzemaekers, M. Gouwy, P. Proost, Neutrophil chemoattractant receptors in health and disease: Double-edged swords. *Cell. Mol. Immunol.* **17**, 433–450 (2020).

46. A. Margraf, C. A. Lowell, A. Zarbock, Neutrophils in acute inflammation: Current concepts and translational implications. *Blood* **139**, 2130–2144 (2022).

47. A. L. Brubaker, J. L. Rendon, L. Ramirez, M. A. Choudhry, E. J. Kovacs, Reduced neutrophil chemotaxis and infiltration contributes to delayed resolution of cutaneous wound infection with advanced age. *J. Immunol.* **190**, 1746–1757 (2013).

48. L. Raffaghello, G. Bianchi, M. Bertolotto, F. Montecucco, A. Busca, F. Dallegri, L. Ottonello, V. Pistoia, Human mesenchymal stem cells inhibit neutrophil apoptosis: A model for neutrophil preservation in the bone marrow niche. *Stem Cells* **26**, 151–162 (2008).

49. B. Feng, X. Feng, Y. Yu, H. Xu, Q. Ye, R. Hu, X. Fang, F. Gao, J. Wu, Q. Pan, J. Yu, G. Lang, L. Li, H. Cao, Mesenchymal stem cells shift the pro-inflammatory phenotype of neutrophils to ameliorate acute lung injury. *Stem Cell Res. Ther.* **14**, 197 (2023).

50. M. Maes, M. Vinken, H. Jaeschke, Experimental models of hepatotoxicity related to acute liver failure. *Toxicol. Appl. Pharmacol.* **290**, 86–97 (2016).

51. J. O'Grady, Timing and benefit of liver transplantation in acute liver failure. *J. Hepatol.* **60**, 663–670 (2014).

52. Y. Luan, X. Kong, Y. Feng, Mesenchymal stem cells therapy for acute liver failure: Recent advances and future perspectives. *Liver Res.* **5**, 53–61 (2021).